12th International Symposium on Turbulence and Shear Flow Phenomena (TSFP12)
Osaka, Japan (Online), July 19-22, 2022

DIRECT NUMERICAL SIMULATION OF TURBULENT FLOW AROUND 3D STEPPED CYLINDER WITH ADAPTIVE MESH REFINEMENT

Daniele Massaro
SimEx/FLOW, Engineering Mechanics
KTH Royal Institute of Technology
SE-100 44 Stockholm, Sweden
dmassaro@kth.se

Adam Peplinski
SimEx/FLOW, Engineering Mechanics
KTH Royal Institute of Technology
SE-100 44 Stockholm, Sweden
adam@mech.kth.se

Philipp Schlatter
SimEx/FLOW, Engineering Mechanics
KTH Royal Institute of Technology
SE-100 44 Stockholm, Sweden
pschlatt@mech.kth.se

ABSTRACT

In the present study, we investigate the turbulent three-dimensional flow around a stepped cylinder, namely two cylinders of different diameters joint at one extremity. We perform a direct numerical simulation with the spectral element code Nek5000 that uses a high order spatial discretisation (the polynomial order is $p = 7$). The adaptive mesh refinement technique is employed in the error-driven meshing procedure, allowing an adequately refined mesh everywhere. We consider the Reynolds number $Re_D = 1000$, based on the large cylinder diameter and the uniform inflow velocity. We compare our results with the previous experimental campaign by Morton & Yarusevych (2014*b*). The results agree very well and we can identify the three main wake regions: the *S*, *N* and *L* cell with a Strouhal number $St_S = 0.408$, $St_N = 0.188$ and $St_L = 0.201$ respectively. The instantaneous mean flow properties are studied showing that the junction dynamics is more similar to the previous laminar studies at $Re_D = 150$ rather than at higher $Re_D = 3900$. Moreover, proper orthogonal decomposition is used to detect the most energetic coherent structures, that resemble the three wake cells.

INTRODUCTION

In the last years, the flow around a stepped (or step-) cylinder has gained more and more interest as it represents a useful model for several engineering applications, *e.g.* the offshore wind turbine towers. It consists of two cylinders with different diameters joint at one extremity and its fluid mechanics is far from being fully understood. For example, three different vortex shedding frequencies have been identified in its wake, counter-intuitively to what one could expect. This aspect has turned out to have relevant side effects on the structural stability of the cylinder itself and further investigations are ongoing.

Unlike the uniform case, for the flow around a single step cylinder, there is an additional parameter to take into account: the ratio D/d between the diameters of the large and small cylinders. Lewis & Gharib (1992) reported a direct and indirect vortex interaction mode for the range $1.14 < D/d < 1.76$ at $67 < Re_D < 200$. The direct mode occurs when $D/d < 1.25$ and it consists of two dominating shedding frequencies, labelled f_S and f_L, corresponding to the small and large cylinder vortex shed respectively. Initially in phase, the two wake cells are connected one by one across the interface. Due to the different frequencies, they move out of phase and at least one half-loop connection between oppositely rotating vortices appears. For $D/d > 1.55$ the indirect interaction generates another distinct region behind the large cylinder. It was named modulation zone by Lewis & Gharib (1992) and is characterized by its own frequency f_N. According to these three dominating shedding frequencies, Dunn & Tavoularis (2006) identified three main regions: the *S* and *L* cells behind the small and large cylinder respectively, and the modulation cell *N* with the lowest shedding frequency ($f_S > f_L > f_N$). The same nomenclature is adopted here. Dunn & Tavoularis (2006) investigated the interactions among the cells for $D/d = 2$ at $Re_D = 150$ through experiments and the results were confirmed through simulations based on Reynolds Averaged Navier-Stokes equations (RANS). On the one hand, it has been observed that the *S*–*N* cell boundary is stable and deflects spanwise into the large cylinder direction; on the other hand, the *N*–*L* cell boundary is unstable. The modulation region boundaries present complicated dynamics as the vortex dislocation occurs. This concept is adapted from solid mechanics and introduced first by Williamson (1989). In the laminar vortex shedding regime Tian *et al.* (2020) investigated the possible loop structures connection. Their observations seem to hold as Re_D increases. Indeed, the three main cells and the dislocation mechanism are still detectable. Nevertheless, the literature lacks results as the Reynolds number increases. Experimentally, Ko & Chan (1992) measured the main integral quantities at $Re_D = 80000$, while Morton *et al.* (2016) presented several results up to $Re_D = 5000$ performing tomographic particle image velocimetry investigation. Regarding the numerical studies, there are unsteady Reynolds Averaged Navier-Stokes (URANS) simulations which have achieved $Re_D = 2000$, *e.g.* Morton *et al.* (2009). Being said that, just recently a first direct numerical simulation has been performed at a high turbulent Reynolds number by Tian *et al.* (2021), without fully resolving the wake region.

In the light of this, we have decided to perform a direct numerical simulation using the spectral element code Nek5000 comparing with the experimental results by Morton & Yarusevych (2014*a*,*b*). Rather than investigating the diameter ratio and Reynolds numbers effect, we have preferred to focus on a single case ($Re_D = 1000$ and $D/d = 0.5$) and provide detailed description of the flow structures. We use a high order polynomial spatial discretisation, guaranteeing an iso-parametric representation of the cylinder. In addition to the high resolution around the cylinder, we use the adaptive mesh refinement (AMR) technique developed by our group, to guarantee a DNS-like resolution in the wake as well. We first provide a general description through instantaneous flow visualisations and measuring the main integral quantities. The mean flow and the turbulent kinetic energy variations along the cylinder are also described. Eventually, we extract the most relevant characteristic features of the flow dynamics using a modal decomposition, *i.e.* proper orthogonal decomposition (POD).

NUMERICAL METHOD

The numerical simulations have been performed using the open-source CFD code Nek5000, Fischer *et al.* (2008). Nek5000 is widely used in the CFD community to perform high fidelity numerical simulations of transitional and high Reynolds incompressible flows. Highly scalable and portable, the code uses the spectral element method (SEM) by Patera (1984) as spatial discretisation. SEM offers minimal dissipation and dispersion, high accuracy and nearly exponential convergence. It can be seen as a high–order finite element method where the solution is represented by Lagrangian interpolants integrated over Gauss-Lobatto-Legendre points (GLL). We use a staggered grid for the pressure to avoid spurious modes and guarantee the Ladyzhenskaya–Babuška–Brezzi (LBB) condition. Adopting the $P_n - P_{n-2}$ formulation, the pressure is discretised on Gauss-Lobatto (GL) points. For time integration, third-order backward differentiation is applied, treating the non-linear term explicitly with an extrapolation formula and the remaining Stokes problem implicitly.

Adaptive mesh refinement

In the spectral element code Nek5000, our group has implemented the adaptive mesh refinement technique (AMR) and extensively used it, see Refs. Offermans *et al.* (2020, 2022); Tanarro *et al.* (2020); Massaro *et al.* (2022). AMR provides a significant flexibility improvement to the meshing procedure, avoiding an over-refinement of the far-field. This results in a significant saving in the number of grid points. As a consequence, on the one hand we can consider a larger computational domain reducing the influence of the boundary conditions, which is critical for incompressible flow simulations. On the other hand, we can increase the Reynolds number or study more complicated geometries. That is the case for the stepped cylinder when an apriori knowledge of the solution is not completely given and an error-driven meshing procedure is pivotal.

In addition to an efficient refinement procedure (here we perform the *h*-type of refinement, where the element is split isotropically), the committed error has to be measured properly. In this regard we have used, the spectral error indicator (sei), which was introduced first by Mavriplis (1989). It measures the truncation and quadrature error for a specified target variable. In the current case, after an in-depth methodology study, the velocity solution field has been used. To explain how it works, let us consider a 1D problem, where $u(x)$ is the exact solution to a system of partial differential equations and u_N is an approximate spectral-element solution with polynomial order N. Let us expand $u(x)$ on a reference element in terms of the Legendre polynomials: $u(x) = \sum_{k=0}^{\infty} \hat{u}_k L_k(x)$, where $\hat{u}_k$ are the associated spectral coefficients and $L_k(x)$ is the Legendre polynomial of order k. The error $\varepsilon = \|u - u_N\|_{L^2}$ consists of two contributions: a truncation error due to the finite number of coefficients in the spectral expansion and the quadrature error. The estimated ε results in:

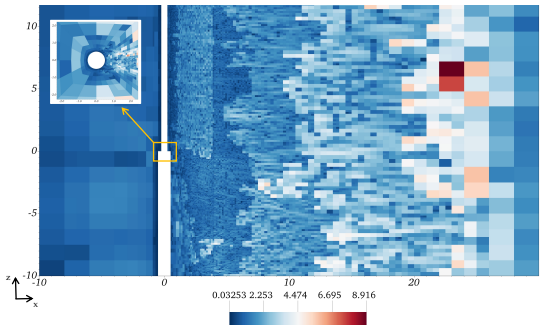

Figure 1. The ratio between the volumetric grid spacing and Kolmogorov length scale l_{vol}/η is shown. We present the planes xy at $z = 0$ and xz at $y = 0$ (zoomed-in window).

$$\varepsilon = \left(\int_N^{\infty} \frac{\hat{u}(k)^2}{\frac{2k+1}{2}} dk + \frac{\hat{u}_N^2}{\frac{2N+1}{2}} \right)^{\frac{1}{2}} \tag{1}$$

where we assume an exponential decay for the spectral coefficients of the form $\hat{u}(k) \approx c \exp(-\sigma k)$. The parameters c and σ are obtained via interpolating in a linear least-squares sense the $\log(\hat{u}_k)$ w.r.t. k for $k \leq N$. The online error measurement ε provides an indication per element at each time step. Afterwards, it is averaged and the meshing procedure stops when the error indicator is converged. Once completed the adaptive mesh design, the final grid is frozen and we start to collect data.

To assess the quality of the mesh, we can evaluate the ratio between the local grid spacing and the Kolmogorov length η. This latter is estimated as $\eta = \nu^{3/4}/\varepsilon^{1/4}$, where the turbulent kinetic energy dissipation ε is computed via statistical analysis. With regard to the grid spacing, in each direction we have: l_i/η, with l_x, l_y and l_z that are the largest spacing in x, y and z directions respectively. As an alternative, we can consider the equivalent volumetric grid spacing l_{vol}/η, where $l_{vol} = (l_x \cdot l_y \cdot l_z)^{1/3}$. In Fig.1, we see how the sei-designed mesh allows to capture the smallest spatial structures close to the cylinder walls, up to Kolmogorov scale. We guarantee a DNS-like resolution in the entire wake region, since at most $l_{vol}/\eta \approx 8$. Please observe that the front part and the cylinder boundary layer are laminar, so the η estimation is meaningless.

Flow configuration

The stepped cylinder is located in the origin of our system of reference that is oriented according to the standard notation for external flow around cylinders, *i.e.* with the z-axis along the cylinder. The diameter ratio is $D/d = 2$, with unitary diameter D. To avoid side and boundary effects the computational box domain is designed with adequate dimensions: $(-10D, 30D)$ in x, $(-10D, 10D)$ in y and $(-10D, 12D)$ in z, where x, y, z are the streamwise, spanwise and vertical directions respectively.

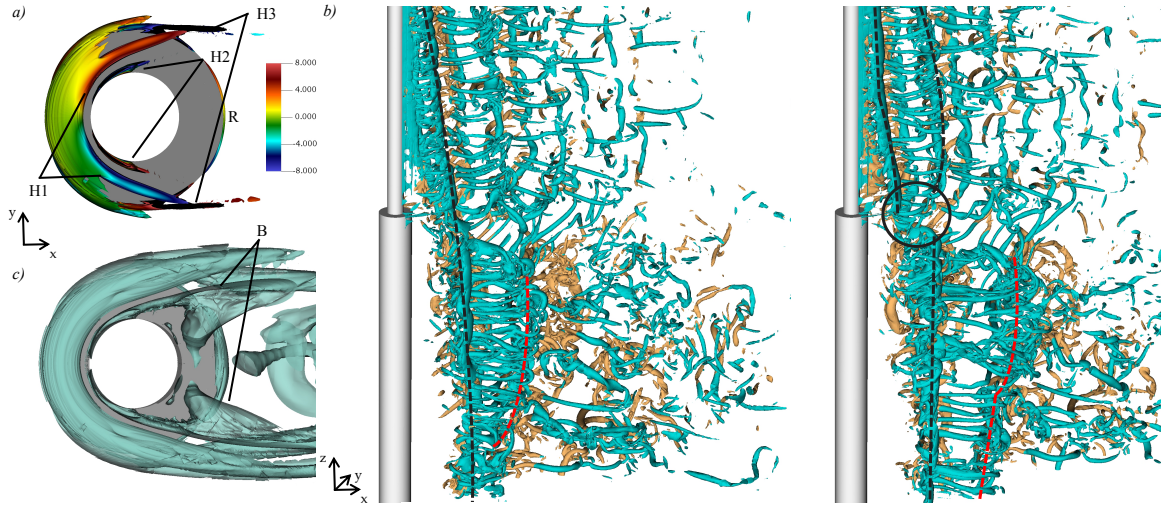

Figure 2. Instantaneous λ_2 visualisations at the junction and in the wake. *a)* The $\lambda_2 = -4$ structures are visualised on the junction ($z = 0$) and coloured with the streamwise vorticity (top view). *b)* The vortex dislocation at *S-N* interface is presented. The green and orange vortices are shed at the negative and positive y respectively; the red lines indicate the oblique shedding occurring in the modulation region. *c)* The $\lambda_2 = -0.2$ structures identify the symmetric base vortices on the back of the junction.

The inflow at $x = -10D$ is set as a Dirichlet boundary condition with the streamwise velocity being a uniform distribution with unitary value $U = u_0 = 1$. The outflow at $x = 30D$ consists of natural boundary condition $(-p\mathbf{I} + \nu\nabla\mathbf{u}) \cdot \mathbf{n} = 0$, where ν is the kinematic viscosity. Considering an infinity long cylinder, symmetry boundary conditions are prescribed at the top/bottom surfaces ($\mathbf{u} \cdot \mathbf{n} = 0$ with $(\nabla\mathbf{u} \cdot \mathbf{t}) \cdot \mathbf{n} = 0$). For the front and back boundaries mixed conditions are used, similar to the open boundary at the outflow, but prescribing zero velocity in non-normal directions. Eventually, for the step cylinder surfaces we have no-slip and impermeable wall.

INSTANTANEOUS FLOW FIELDS

We qualitatively describe the main structures present in the flow field using the λ_2 criterion by Jeong & Hussain (1995). The convention for the vortices classification follows Tian *et al.* (2021).

First, we focus on the junction region. In the front part, the formation of streamwise vortices is similar to the top-end plate of a finite-length cylinder, see Zdravkovich *et al.* (1989). Figure 2-*a* shows that the impingement of the flow, due to the presence of the small cylinder, together with the leading-edge separation is mainly responsible for the horseshoe vortex H1 formation. This generates a recirculating pressure bubble with its core at $(x/D, y/D, z/D) \sim (-0.354, 0, 0.046)$. Other typical structures are the edge vortices H3, always visible on the free-end surface and typically named tip-vortices. The blockage and the H1 rotation induce the incoming flow to divert laterally, where it spills over the edges of the step. Here, it rolls up into two streamwise edge-vortices, see Fig.2-*a*. These observations agree with the measurements first made by Dunn & Tavoularis (2006) at lower $Re_D = 150$. Recently, Tian *et al.* (2021) points out some additional structures at $Re_D = 3900$. The first one is a vortex (H4) which appears upstream of H3 and rotates in the same direction as H1. At the current Reynolds ($Re_D = 1000$) the mentioned mechanism is not present on the junction front. The boundary layer separation occurs downstream and other smaller turbulent eddies do not appear around the junction. Figure 2-*a* shows in a clear way that the horseshoe vortex H4 is not present. The leading separation generates only H1. This difference is confirmed by looking at time-averaged streamlines in figure 3-*b*. That has a relevant consequence in the H3 formation. Indeed, Tian *et al.* (2021) report that the edge vortex H3 is a horseshoe vortex caused by the backward flow below the junction vortex H1. The H4-H1 vortex bridge and the hairpins observed at $Re_D = 3900$ are identified as responsible for H3. At the current Reynolds number, we assert that the mechanism which generates the edge vortices agrees with the Dunn & Tavoularis (2006)'s observations at lower $Re_D = 150$. The leading edge separation with the small cylinder impingement drives the recirculating vortex H1 formation that laterally deviates the incoming flow shaping the H3s. The second type of structure observed by Tian *et al.* (2021) is named H2 and is present at the current $Re_D = 1000$ too. These are horseshoe vortices that evolve at the base of the small cylinder with cross-flow widths that continue to increase downstream, as for H1 (see Fig.2-*a*). All the three horseshoes (H1, H2, H3) in the forepart of the step surface ($x/D < 0$), are stable and with small fluctuations in time. On the contrary, the back structures are weaker and more difficult to identify. Differently to Tian *et al.* (2021), which uses time-average λ_2 structures to observe them, we manage to visualise the instantaneous base vortices B1 and B2 (Fig.2-*c*). Eventually, Tian *et al.* (2021) points out a backside vortex that here appears at a different location. We name it ring-vortex R and its core is in the back part of the junction at $(x/D, y/D, z/D) \sim (0.39, 0, 0.02)$. R is formed by the H3 vortices that roll up around the edges and split before diverging laterally. The vortex segment which remains attached to the edges generates R. The low-pressure region behind the cylinder stabilises R on the back, whereas the strong flow advection interrupts the ring connection laterally.

With regards to the coherent structures in the wake region, we observe several streamwise spaghetti-like structures on top of the typical vertical vortices (whose axis is z-oriented), see Fig.2-*b*. In laminar vortex shedding, the z vortices are distinguishable making the vortex dislocations investigation simple. This is not the case for a turbulent wake. Nevertheless, since the *S-N* boundary is stable, it is possible to observe when the dislocation occurs. Figure 2-*b* identifies the initial in phase vortex shed by the cylinder and the consequent dislo-

Table 1. Strouhal numbers for different probe locations. The results from the current study and Morton & Yarusevych (2014*b*) are reported on the first and second rows respectively.

St_1	St_2	St_3	St_4	St_5
0.408	$0.41-0.22$	0.188	$0.19-0.20$	0.201
0.398	–	0.189	–	0.198

cation. The dashed-red lines point out the oblique vortex shedding which creates the intermediate modulation region with a triangular-like shape. Contrary to the upper interface, the *N*-*L* layer is unstable and makes it challenging to study. Nevertheless, we believe that is possible to find the *N* and *L* cells' location and monitor the shedding through a modal decomposition analysis. In the current study, we rely on the proper orthogonal decomposition (POD) of the flow to identify the most energetic structures in the wake and characterize the different shedding regions. The results are discussed below.

QUANTITATIVE ANALYSIS

The quantitative description of the flow begins with measurements of the velocity signal from virtual probes located in the flow and the evaluation of the relevant integral quantities. The probes are placed at specific locations, following Morton & Yarusevych (2014*b*)'s experimental setup. We also measure the drag coefficient of each cylinder and provide a brief overview of some relevant statistical quantities.

Velocity probes measurements

The previous studies indicate that three distinct vortex shedding cells develop in the wake and eachone is characterised by different a frequency. We use spectral analysis of velocity signals to determine the vortex shedding frequency and investigate how it varies for different vertical locations.

The spectral analysis results are compared with previous experiments carried out by Morton & Yarusevych (2014*b*) at the same $Re_D = 1000$. In this regard, we locate five virtual velocity probes at the same locations. The time signals are acquired with the sampling frequency $f_s = 100Hz$. It definitely meets the Nyquist theorem requirements, since the highest frequency of the flow is supposed to be the small cylinder vortex shedding at $f_s \approx 0.4Hz$. The time-averaging interval is long enough to capture the slowest dynamics exploring over ≈ 200 *S*-cell vortex shedding periods. The virtual probes are located at $z_1/D = 4$, $z_2/D = -1$, $z_3/D = -3$, $z_4/D = -5$ and $z_5/D = -9$. The streamwise and spanwise locations are the same for all of them, $x/D = 5$ and $y/D = 0.75$ respectively. The resulting streamwise velocity spectra are presented in Fig. 4.

The Strouhal number is defined as $St = fD/u_0$ and the agreement with the experimental measurements is excellent. Each wake region is characterized by a distinct shedding frequency and exhibits a single peak: $St_S = 0.408$, $St_N = 0.188$ and $St_L = 0.201$ for the *S*, *N* and *L*-cell respectively (see Fig.4-a,b,d). At the boundary between the *S* and *N* cells (z_2), two dominant peaks are related to the Strouhal numbers that correspond to the adjacent cells (Fig.4-c). Similarly, we observe a double peak at the *N*-*L* boundary. Morton & Yarusevych (2014*b*) uses the velocity streamwise spectra to analyse how the energy context varies in the different cells and the extension of the cell. An analogous observation can be deducted by our study: at the interface Fig.4-*b* the energy content is diminished substantially compared to that within the single cells Fig.4-a,c. Nevertheless, a more detailed discussion about the energy content for each cell is carried out in the POD section.

Integral quantities

In the current section we report the dimensionless drag coefficient C_D, *i.e.* the horizontal component of the aerodynamic force normalised with $1/2\rho u_0^2 D L_z$, with L_z being the vertical cylinder length. The aerodynamic force is computed online as the sum of the viscous and pressure contributions $\mathbf{F_a} = \int_S -p\mathbf{n} + \boldsymbol{\tau}\mathbf{n}\ \mathrm{d}\delta S$ with S the cylinder surface, p the pressure, $\mathbf{n}$ the vector normal to the cylinder surface and τ the viscous stress $\tau_{ij} = \mu \partial u_i/\partial u_j$. After the normalisation, the drag coefficient is time averaged to yield $\overline{C_D}$. For symmetry reasons, the lateral y component of the aerodynamic force, and its normalised formulation C_y, is expected to be zero for an infinitely long simulation. In the current study they result $\overline{C_{yS}} = 0.0017$ and $\overline{C_{yL}} = 0.00053$, assessing the well temporal convergence for our statistics. The mean drag coefficients are $\overline{c_D} = 1.1084$ and $\overline{c_D} = 0.9083$ for the small and large cylinder respectively. Both the standard deviations are approximately $\sigma_{c_D} \approx 0.016$. As expected in the Re_D range $100 < Re_D < 10^5$ the drag coefficient is $c_D \approx 1$. The pressure contribution is dominant (around 90%) w.r.t. the viscous one for both cylinders.

Mean flow quantities

The mean streamwise velocity profiles are shown in Fig.3-a at different z locations. The cylinder is immersed in a uniform velocity field that forms a laminar boundary layer and eventually separates. The flow evolves detached from the surface due to an adverse pressure gradient. The phenomenon occurs similarly for the large and small cylinders. On the junction, the mean streamwise velocity shows a sharp contraction of the layer before the separation. In a similar way to the free-end uniform cylinder, the downwash region is visible behind the junction, see Fig.3-*b*. In the front junction part, the mean statistics confirm what has been observed via instantaneous λ_2 structures: the flow is lifted on the top lead by the leading-edge vortex H1. Then, the impingement at the base of the small cylinder pushes the flow downstream on the junction.

The core of the recirculating vortex H1 is located at $(x/D, y/D, z/D) = (-0.354, 0, 0.046)$. In agreement with Dunn & Tavoularis (2006) and contrary to Tian *et al.* (2021), H1 is the only vortex present in the front part, see the mean velocity streamlines in 3-*b*. The H2 vortex cores are not visible here because the cross-section is taken for $y = 0$ and H2 structures are developed on the sides. In the back, the streamlines confirm that no backside vortex is present. In fact, the ring vortex is visible and located at $(x/D, y/D, z/D) = (0.39, 0, 0.02)$, see Fig.3-*b*.

Figure 3-c shows a spatial map of the mean turbulent kinetic energy k, which is proportional to the trace of the Reynolds stress tensor. We observe the symmetry w.r.t. to the streamwise direction supporting the adequacy of the statistical sample. To the authors' knowledge, this is the first-ever k-map for this flow configuration. The white line defines the iso-contour $k = 0$ and points out the region where the flow is laminar. The "bat"-shape varies with the vertical positions, becoming more irregular at the junction. Since $Re_D = 2Re_d$ we observe different tails' elongation, but both have a similar long shape with a more extended laminar region for the large cylin-

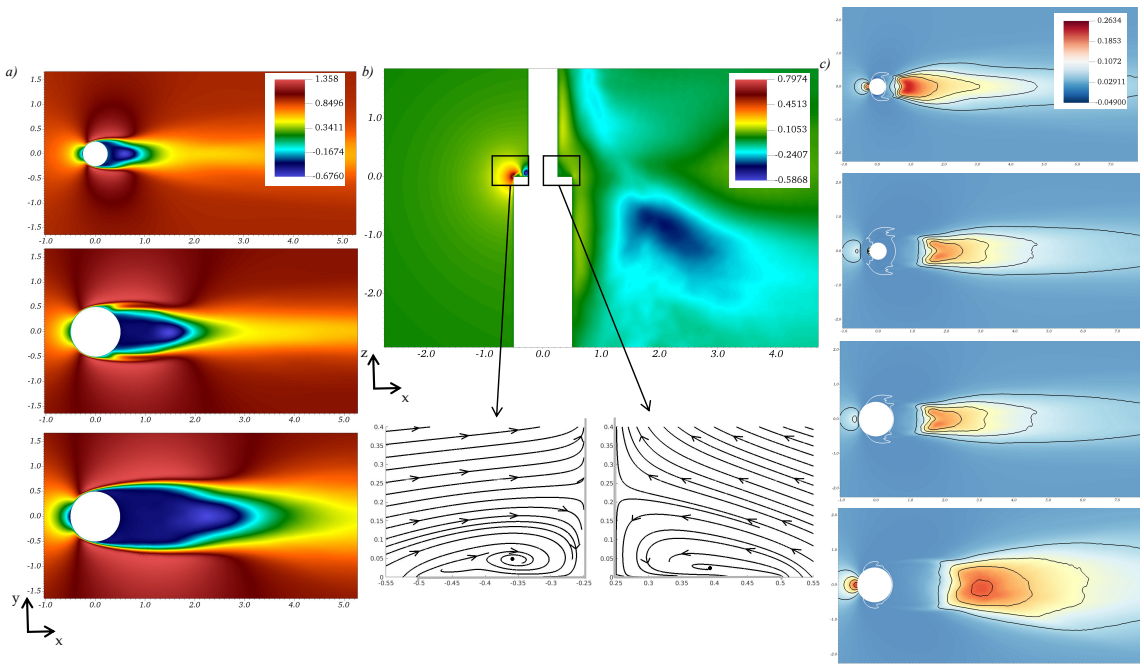

Figure 3. Selection of time-averaged quantities. *a)* The mean streamwise velocity is presented at different z location, from the top $z/D = 9$, $z/D = 0$ and $z/D = -9$. *b)* The mean vertical velocity component is shown. The in-plane streamlines for the mean x velocity component are illustrated in the front/back junction regions. *c)* The mean turbulent kinetic energy map is shown at $z/D = 9$, $z/D = 0.01$, $z/D = 0$ and $z/D = -9$.

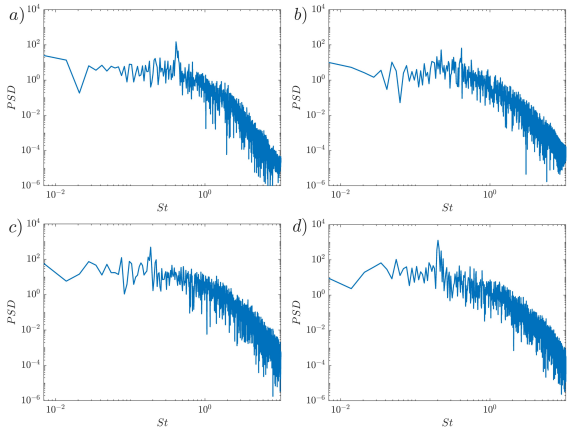

Figure 4. The power spectral density of the streamwise velocity component at locations specified above in the text: z_1, z_2, z_3 and z_5. The log-log plot reports the Strouhal number along the x axis.

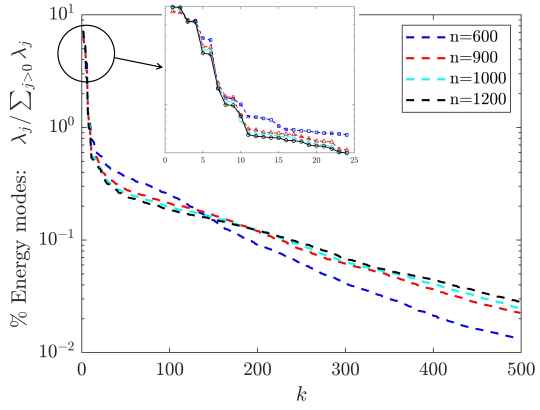

Figure 5. The percentage energy contribution of each k mode for different number of snapshots n.

der. At $z = 0$, we have a triple peak structure that gets even more contorted on the junction surface ($z = 0.01$).

PROPER ORTHOGONAL DECOMPOSITION

The POD performs the modal decomposition of the nonlinear flow minimizing the residual energy between the snapshots and its reduced linear representation. They are constructed to be the orthogonal basis which represents the optimal projection, in energy terms, of the most important dynamical features. It was first introduced in the fluid-mechanics context by Lumley (1970) and the approach is referred as classical POD. Here we use the snapshot POD, developed by Sirovich (1987) to handle the analysis of three-dimensional flows with a big set of grid points.

We collect a large number of snapshots that are sampled according to the Nyquist criterion and for a time interval sufficiently long to embed the slowest frequency. The convergence is observed in Figure 5. According to the adopted convection, mode 0 corresponds to the expected mean value of the flow and the agreement with the estimated mean value is excellent. The first pair of travelling modes, namely the modes 1 and 2 which have 90-degree phase shift, correspond to large cylinder modes in the L cell region. They account each for around the $\sim 7\%$ of the total (fluctuating) energy. The second pair, modes 3 and 4, identify the S region behind the small cylinder contributing each for the $\sim 5.5\%$ of total energy. The N-cell region (modes 5 and 6) have an energy contribution that is half of the previous pair $\sim 2.8\%$. The results agree with a previ-

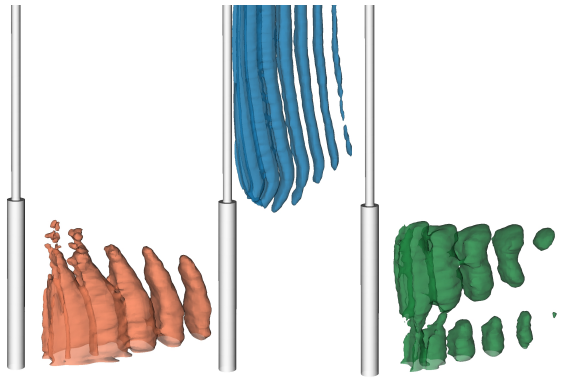

Figure 6. Velocity magnitude iso-surfaces for the first (*orange*), third (*blue*) and fifth (*green*) POD mode.

ous study by Morton & Yarusevych (2014*a*) where the POD has been performed based on planar velocity data obtained via Particle Imagine Velocimetry (PIV). For the mode 5 we do not see any interactions between *S* and *N* cells, which are characterized by a stable interface; unlike the *N*-*L* layer. Moreover, the POD helps to identify the modulation region extension and its shape. This latter agrees well with the visualisations carried out by Dunn & Tavoularis (2006), showing a triangle-like shape that is persistent in the turbulent regime. Finally, we would like to comment on the single mode 7. It has an energy contribution larger than the 1% and seems related to the downwash phenomenon which occurs behind the junction. It has a frequency that agrees with the previous estimation by Morton & Yarusevych (2014*b*). As we are aware that each POD mode does not correspond to a single frequency in time, further investigations are ongoing through other modal decompositions, such as dynamic mode decomposition (DMD), which allows having every mode with a single temporal frequency.

CONCLUSIONS

The study performs a DNS of a turbulent flow around the three-dimensional stepped cylinder at $Re_D = 1000$ by means of adaptive mesh refinement (AMR). The AMR enables to have an accurate solution for the entire domain, with a volumetric grid spacing less than 10 Kolmogorov length scales everywhere. The results are compared with the experiments by Morton & Yarusevych (2014*b*) showing an excellent agreement. The three *S*, *N* and *L* wake regions are confirmed in the turbulent regime with a stable interaction at the *S*-*N* interface, but unstable at the *N*-*L* boundary. The proper orthogonal decomposition (POD) identifies these three coherent regions and allows for assessing their energy contributions. In addition, even if less energetically relevant, the downwash mode is observed. We also discuss some of the mean flow properties. The mean turbulent kinetic energy k shows how the flow evolves differently around the cylinder according to the z locations. In the future, a more insightful and detailed statistical description, *e.g.* considering the k budgets, might help to improve our understanding of such a flow configuration.

ACKNOWLEDGEMENTS

This study was funded by Knut and Alice Wallenberg Foundation and the Swedish e-Science Research Centre (SeRC); enabled by resources provided by the Swedish National Infrastructure for Computing (SNIC).

REFERENCES

Dunn, W. & Tavoularis, S. 2006 Experimental studies of vortices shed from cylinders with a step-change in diameter. *J. Fluid Mech.* **555**, 409–437.

Fischer, P., Kruse, J., Mullen, J., Tufo, H., Lottes, J. & Kerkemeier, S. 2008 Nek5000: open source spectral element CFD solver. https://nek5000.mcs.anl.gov/ .

Jeong, J. & Hussain, F. 1995 On the identification of a vortex. *J. Fluid Mech.* **285**, 69–94.

Ko, N. W. M. & Chan, A. S. K. 1992 Wakes behind circular cylinders with stepwise change of diameter. *Exp. Therm. Fluid Sc.* **5**, 182–187.

Lewis, C.G. & Gharib, M. 1992 An exploration of the wake three dimensionalities caused by a local discontinuity in cylinder diameter. *Phys. Fluids* **4**, 104–117.

Lumley, J. L. 1970 Stochastic tools in turbulence. *Academic* .

Massaro, D., Peplinski, A. & Schlatter, P. 2022 Interface discontinuities in spectral-element simulations with adaptive mesh refinement. In *Spect. High Ord. Meth. Part. Diff. Eq. - ICOSAHOM 2021 (submitted)*. Springer.

Mavriplis, C. 1989 Nonconforming discretizations and a posteriori error estimators for adaptive spectral element techniques. PhD thesis, MIT, USA.

Morton, C. & Yarusevych, S. 2014*a* On vortex shedding from low aspect ratio dual step cylinders. *J. Fluids Struct.* **44**, 251–269.

Morton, C. & Yarusevych, S. 2014*b* Vortex dynamics in the turbulent wake of a single step cylinder. *J. Fluids Eng.* **136** (3).

Morton, C., Yarusevych, S. & Carvajal-Mariscal, I. 2009 Study of flow over a step cylinder. *Appl. Mech. Mater.* **15**.

Morton, C., Yarusevych, S. & Scarano, F. 2016 A tomographic particle image velocimetry investigation of the flow development over dual step cylinders. *Phys. Fluids* **28**.

Offermans, N., Massaro, D., Peplinski, A. & Schlatter, P. 2022 Error-driven adaptive mesh refinement for unsteady turbulent flows in spectral-element simulations. *Comp. Fluids (submitted)* .

Offermans, N., Peplinski, A., Marin, O. & Schlatter, P. 2020 Adaptive mesh refinement for steady flows in nek5000. *Comp. Fluids* **197**, 104352.

Patera, A.T. 1984 A spectral element method for fluid dynamics: Laminar flow in a channel expansion. *J. Comput. Physics* **54** (3), 468–488.

Sirovich, L. 1987 Turbulence and the dynamics of coherent structures. part i: Coherent structures. *Q. Appl. Math.* **45**.

Tanarro, A., Mallor, F., Offermans, N., Peplinski, A., Vinuesa, R. & Schlatter, P. 2020 Enabling adaptive mesh refinement for spectral-element simulations of turbulence around wing sections. *Flow, Turb. Combus.* **105**, 415–436.

Tian, C., Jiang, F., Pettersen, B. & Andersson, H. I. 2020 Vortex dislocation mechanisms in the near wake of a step cylinder. *J. Fluid Mech.* **891**, A24.

Tian, C., Jiang, F., Pettersen, B. & Andersson, H. I. 2021 Vortex system around a step cylinder in a turbulent flow field. *Phys. Fluids* **33**.

Williamson, C. H. K. 1989 Oblique and parallel modes of vortex shedding in the wake of a circular cylinder at low reynolds number. *J. Fluid Mech.* **206** (3), 579–627.

Zdravkovich, M., Brand, V., Mathew, G. & Weston, A. 1989 Flow past short circular cylinders with two free ends. *J. Fluid Mech.* **203**, 557–575.